Article

Simulation and Analysis of Fluid–Solid–Thermal Unidirectional Coupling of Near-Space Airship

Jiwei Tang [1] , **Weicheng Xie** [2,*] , **Xiaoliang Wang** [1] **and Cheng Chen** [1]

1   School of Aeronautics and Astronautics, Shanghai Jiao Tong University, Shanghai 200240, China
2   Aerospace System Engineering Shanghai, Shanghai 201108, China
*   Correspondence: xieweicheng@asesspace.com

Abstract: Based on the biaxial experiment data of the membrane material under hot and cold conditions, the mechanical properties calculation model of envelope material was established with consideration of the effects of varying stress ratios, stress magnitudes and temperatures on the mechanical properties of near-space airship material. Using the heat source model, Computational Fluid Dynamics (CFD) simulation, User-Defined Function (UDF), structural finite element analysis software and the user subroutine of an airship to define the behaviour of fabric material, the fluid–structure–thermal coupling model of airship envelopes was established. In addition, a near-space airship was selected as the research subject to calculate the diurnal temperature differences during the summer solstice and analyse the diurnal temperature distribution of the envelope. Under controlled environmental conditions, the deformation law of the near-space airship under the influence of fluid–structure–thermal coupling was calculated and summarised. The present fluid–solid–thermal coupling model takes into account the anisotropy of materials, temperature, stress magnitude, stress ratio and other influencing factors, which can more accurately reflect and predict the stress–strain distribution and the deformation law of near-space airships.

Keywords: mechanical properties; near-space airship; fluid–solid–thermal coupling; simulation

1. Introduction

For a large near-space airship [1,2], the envelope material is not only directly affected by environmental temperature but also by local radiation, cloud reflection, internal and external heat transfer and convective heat transfer [3,4]. The temperature difference of near-space airship envelope material can reach more than 100K [5–7], such as the temperature difference between day and night near the installation of solar panels in the envelope. The change of buoyancy and envelope stress caused by temperature change will have a great influence on the normal operation of the near-space airship. Finally, the local overheating and cooling will even lead to the deformation and rupture of the envelope. In addition to thermal factors, airships are also affected by fluid pressure and their own material properties. Therefore, fluid–solid–thermal coupling analysis of near-space airships is of great significance to avoid overheating and improve the overall design of near-space airships.

The research on heat source models of near-space airships has been relatively developed, but there have been few experimental studies [8–12]. This is due to the intensive requirements of trials coupled with the strict confidentiality of many studies, resulting in more difficult access to open experimental research data. At present, most of the experimental studies simulate the stratospheric environment and study the small aerostat model. Harada [13] established a simplified thermal model and verified it through the thermal measurement of a 25 m/35 m airship. The effectiveness of the model was verified through a series of flight tests of small aircraft. Cheng X.T. [14] established a theoretical model for thermal analysis under various radiation conditions, carried out numerical simulation using commercial software and designed a research test on the thermal characteristics of a

1.5 m-long aerostat, which proved the accuracy of the theoretical model by comparison. Bruce [15] conducted a thermal simulation of an infrared aerostat with a diameter of 0.4 m placed in a large inflatable tank with a cold top wall and adiabatic side wall and studied the local Nusselt number under different conditions. Li D.F. [16] established a simulation test device for the transient heat transfer characteristics of an airship model and measured and obtained transient temperature change data of envelope materials and helium gas in different parts of the airship model under simulated solar irradiation and different airflow conditions.

It is worth noting that although there are many pieces of research on the thermal characteristics of near-space airships [17–21], most of the models established by scholars do not consider the transmission characteristics of envelope materials and ignore the direct influence of external heat sources on the thermal characteristics of the inner filled gas. A large part of near-space airship materials has transmission. The main heat source factors considered by different scholars are different; the empirical formulas are different, and some of the empirical formulas are quite different from the actual situation. In addition, the comprehensive factors such as environmental parameters and analysis methods lead to a big difference in the calculation results of the model. Therefore, when establishing the thermal model, it is necessary to comprehensively consider the influence rules of different factors on the thermal characteristics of the aerostat. The general CFD software can be used to replace part of the empirical formula to improve the accuracy so that the established model has general engineering value and significance.

Cheng C. and Wang X.L. realised the simulation of the mathematical model of the thermal characteristics of the aerostat mentioned above by means of numerical simulation and calculated the envelope unit and time as discrete quantities [22]. The model considers the transmission characteristics of the airship envelope and can predict the thermal characteristics of the airship envelope more accurately and comprehensively. The simulation calculation of the simulation model test of the thermal characteristics of the aerostat in Li D.F.'s doctoral thesis [14] was carried out, and the numerical calculation results were compared with the experimental results in the literature. The results show that the thermal characteristics model, numerical calculation program and method of aerostat established by this method are accurate. On this basis, Wang [23] compiled the mathematical model of the thermal characteristics of the airship into a UDF subroutine, realised the loading of the heat source around the airship by invoking the user subroutine with CFD software and replaced the mathematical calculation model of the natural convective heat transfer of gas inside the envelope and the forced convective heat transfer outside the envelope with the CFD heat balance equation. The calculation accuracy of the model is further improved. Through numerical simulation analysis, the diurnal variation characteristics of the envelope temperature of the conventional near-space airship were obtained.

The surface temperature of the near-space airship envelope will affect the mechanical properties of the envelope, and the local overheating or undercooling caused by the thermal environment will lead to the local deformation of the envelope, affecting the structural safety of the airship. In view of this, thermo-solid coupling analysis is needed to estimate the temperature and the corresponding stress–strain law of the airship envelope at different times. Fluid-structure coupling of near-space airships has been studied more than thermal-structure coupling. For example, Wang X.L. [24] developed a nonlinear dynamic fluid-structure staggered integral coupling method to analyse fluid-structure coupling characteristics of large flexible inflatable structures like near-space airships based on fluid dynamics calculation software FLUENT and structural analysis software ABAQUS. Bessert [25] proposed a coupling method of VSAERO (aerodynamic analysis method based on potential flow theory) and ABAQUS (structural analysis software) to solve the static aeroelasticity of airships. Omari [26] used the ALE method to solve Navier–Stokes's three-dimensional compressible equation and calculated the static aeroelasticity of ellipsoid shape with a length of 1.37 m, slenderness ratio of 6 and angle of attack of 20. Liu J.M. [27] established a fluid-structure coupling calculation method for large deformation of mem-

brane structure in a three-dimensional flow field and carried out fluid-structure coupling analysis for the near-space airship. There are few studies on the thermo-solid coupling of near-space airships. Dai Q.M. [28] realised the coupling analysis of steady-state heat transfer and the fluid and structural deformation of near-space airships by using ANSYS WORKBENCH, revealing the influence of wind speed and diurnal temperature changes on the stress and strain of the airship airbag envelope. Specifically, fluid analysis was done using FLUENT, and structural deformation analysis was performed using the APDL solver. However, the coupling model does not consider the effect of anisotropy and temperature on the mechanical properties of the envelope.

The main innovation of this work is that the fluid–solid–thermal coupling analysis of the near-space airship was realised based on the high and low-temperature biaxial tensile test data and took into account the anisotropy of materials and the influence of temperature on the mechanical properties of the envelope material. Firstly, the fitting estimation formula of elastic modulus and Poisson's ratio of UN-5100 envelope material at -33–$80\ ^\circ\text{C}$ is provided, and the calculation model of mechanical properties of envelope material at high and low temperatures is established. Secondly, based on the work done by Cheng C. [22] and Wang X.L. [23,24], the heat source model of the airship envelope considering different radiation conditions is introduced. Then, the VFABRIC subroutine was used to simulate the effects of different stress ratios, stress sizes and temperatures on the mechanical properties of near-space airship materials. Finally, a near-space airship with a length of 140 m and a maximum diameter of 38 m was selected as the research object. Based on the heat source model and CFD software, the force and deformation law of the near-space airship under the influence of fluid–solid–thermal coupling was analysed under the set environmental conditions. The diurnal temperature difference of the airship on the summer solstice was calculated, and the diurnal temperature distribution law of the envelope was analysed and summarised.

2. Methodology

2.1. Material Model

According to the stress–strain curve of the biaxial tensile test, a univariate quadratic polynomial can be used to fit the curve:

$$\sigma = \alpha_1 \varepsilon^2 + \alpha_2 \varepsilon + \alpha_3 \tag{1}$$

The elastic modulus at any moment can be obtained by deriving ε of the above equation in warp and weft directions. However, the elastic modulus obtained by this method only considers the effect of the stress in one direction. In fact, the stress in warp and weft directions will both affect the elastic modulus of the material. Therefore, the elastic modulus can be assumed to be E_x and E_y, and the below bivariate quadratic polynomial can be obtained:

$$E_x = \lambda_0 + \lambda_1 \sigma_x + \lambda_2 \sigma_x^2 + \lambda_3 \sigma_y + \lambda_4 \sigma_y^2 + \lambda_5 \sigma_x \sigma_y \tag{2}$$

$$E_y = \kappa_0 + \kappa_1 \sigma_x + \kappa_2 \sigma_x^2 + \kappa_3 \sigma_y + \kappa_4 \sigma_y^2 + \kappa_5 \sigma_x \sigma_y \tag{3}$$

where λ_{0j}, k_{0j} and η_{0j} ($j = 0 \ldots 5$) are evaluation parameters. Significances of each monomial term in the above bivariate quadratic polynomial are shown in Figure 1. Where 'λ_5' and 'k_5' in the above bivariate quadratic polynomial evaluate the effect of both δ_x and δ_y on the elastic modulus E_x and E_y.

$$
\begin{aligned}
E_x &= \boxed{\lambda_0} + \lambda_1\,\sigma_x + \lambda_2\,\sigma_x^2 + \lambda_3\,\sigma_y + \lambda_4\,\sigma_y^2 + \lambda_5\,\sigma_x\,\sigma_y \\
E_y &= \boxed{\kappa_0} + \kappa_1\,\sigma_x + \kappa_2\,\sigma_x^2 + \kappa_3\,\sigma_y + \kappa_4\,\sigma_y^2 + \kappa_5\,\sigma_x\,\sigma_y
\end{aligned}
$$

☐ Evaluate the Effect of Warp Stress on the Modulus

⬚ Evaluate the Effect of Weft Stress on the Modulus

⬓ Evaluate the Effect of Both Warp and Weft Stress on the Modulus

Figure 1. Significance of each monomial term.

The initial Poisson's ratio v_{yx} and v_{xy} can be calculated using the following formula:

$$
\nu_{yx} = \left(\frac{\sigma_x}{E_x} - \varepsilon_x \right) \frac{E_y}{\sigma_y} \tag{4}
$$

$$
\nu_{xy} = \frac{E_x}{E_y} \nu_{yx} \tag{5}
$$

The above initial Poisson's ratio can be fitted using the bivariate quadratic polynomial:

$$
\nu_{yx} = \eta_0 + \eta_1\sigma_x + \eta_2\sigma_x^2 + \eta_3\sigma_y + \eta_4\sigma_y^2 + \eta_5\sigma_x\sigma_y \tag{6}
$$

At the $-33\,^\circ\text{C}$ to $80\,^\circ\text{C}$ temperatures, the UN-5100 envelope material stress–strain data is processed and calculated, and 18 optimisation parameters can be obtained at the corresponding temperature, as shown in Table 1. According to the parameters of the 18 elastic modulus and Poisson's ratio polynomial equations under various temperature conditions, the VFABRIC subroutine can be compiled to obtain a subroutine that could reflect the mechanical parameters of envelope material under high- and low-temperature environments.

Table 1. Parameters of the simulation environment.

Temperature (°C)	−33	3	23	40	80
λ_0	3669.515	2296.417	1715.832	1373.241	1300.335
λ_1	−257.781	−174.32	−109.514	−56.4565	13.3424
λ_2	−2.48195	0.485099	−0.27352	−0.72883	−1.14517
λ_3	9.249948	6.827669	5.279409	3.7769	−0.71296
λ_4	1.411409	0.650474	0.536042	0.449718	−0.33591
λ_5	0.539084	0.091826	0.127741	0.117449	−0.82441
κ_0	2869.423	1792.312	1429.07	1245.06	1237.787
κ_1	0.447077	0.529999	−0.01938	−0.51707	0.6388
κ_2	−114.703	−79.9611	−43.7049	15.6374	−6.46238
κ_3	0.291252	0.269617	0.142972	0.02213	−0.11448
κ_4	3.601823	1.915789	1.823383	1.783014	0.157013
κ_5	0.173065	0.227971	0.136431	0.0114	−0.37252
η_0	0.012636	0.2625335	0.40475	0.500943	0.5663782
η_1	0.042854	0.037915	0.02569	0.015421	0.011972
η_2	0.06888	−0.01384	−0.02771	−0.03523	−0.08995
η_3	0.000383	−0.00078	−0.00098	−0.00143	−0.00554
η_4	−0.00037	0.0013439	0.001955	0.002122	0.0006894
η_5	−0.00774	−0.002531	−0.00193	−0.00095	0.0097954

2.2. Thermal Model

Large near-space airships are particularly sensitive to the stratospheric thermal environment. Figure 2 lists the main factors influencing the thermal sensitivity of airships in near space. For thermal radiation, the object with a spectral absorption ratio independent of wavelength is called a grey body. Gray bodies do not absorb all the energy of thermal radiation, and some of it is reflected away. Compared with the grey body, a black body is the standard object in the field of thermal radiation, can completely absorb all external

electromagnetic radiation, and there will be no reflection and transmission. The main thermal factors of an airship in the stratosphere are solar long-wave radiation, short-wave radiation and convective heat transfer. Solar long-wave radiation includes earth radiation, atmospheric radiation around the airship and radiation heat transfer between envelope material units. Short-wave solar radiation includes direct solar radiation, scattered radiation from the sky and reflected radiation from the earth and clouds.

Figure 2. Near-space airship thermal environment.

2.2.1. Earth Radiation

After receiving solar energy, the ground continuously releases its own energy to the atmosphere in the form of radiation. This radiation is called ground radiation or ground long-wave radiation, as this band belongs to the infrared region. Airships are treated as grey bodies in the earth's long-wave radiation. The mathematical model of ground long-wave radiation calculation is:

$$I_{GREarth} = \varepsilon_{Earth}\sigma_S\tau_{atmIR}T_{Earth}^4 \tag{7}$$

where ε_{Earth} is the average emissivity of the earth, 0.92, Stefan–Boltzmann constant $\sigma_S = 5.67 \times 10^{-8}$ W/(m^2·K4). T_{Earth} is the equivalent temperature of the grey body on the earth's surface [29], 255 K. τ_{atmIR} is the transmittance of long wave radiation [16], which can be calculated by the following formula:

$$\tau_{atmIR} = 1.716 - 0.5\left[e^{0.65\frac{P_a}{P_0}} + e^{-0.095\frac{P_a}{P_0}}\right] \tag{8}$$

where P_a is the atmospheric pressure around the airship, P_0 is the atmospheric pressure at the surface of the Earth.

$$Q_{GREarth,i} = \frac{1}{2}\varepsilon_{skinex}\left(I_{GREarth} - \sigma_s T_{skin,i}^4\right)(1 + cos\beta_2)A_{skin,i} \tag{9}$$

where ε_{skinex} is the infrared emissivity of the outer surface of the near-space airship. $T_{skin,i}$ is the temperature of the *i*-th envelope unit. Where β_2 is the included angle between the normal direction and gravity direction of the surface material unit of the near-space airship [20]. $A_{skin,i}$ is the area of the i-th envelope unit.

2.2.2. Atmospheric Radiation

Atmospheric radiation is a cold source for airships at low temperatures at night and is the main thermal influence factor of airship surface envelope; it is considered a black body.

$$I_{IRSky} = \sigma_s T_{sky}^4 \tag{10}$$

where T_{sky} is the equivalent radiation temperature of the atmosphere around the airship, which can be calculated by the following formulas:

$$T_{sky} = \tau_{sky}^{\frac{1}{4}} T_a \tag{11}$$

$$Q_{IRSky} = \frac{1}{2}\varepsilon_{skinex}\left(I_{IRSky} - \sigma T_{skin,i}^4\right)(1 - cos\beta_2)A_{skin,i} \tag{12}$$

2.2.3. Direct Solar Radiation

Solar radiation intensity can be calculated by the following formula:

$$I_0 = S_0\left(\frac{1 + ecos\phi_r}{1 - e^2}\right)^2 \tag{13}$$

where e is the eccentricity of the orbit, 0.016708. S_0 is 'solar constant', 1367 W/m^2. ϕ_r is sun's angle:

$$\phi_r = 2\pi\frac{n_j - 4}{365} \tag{14}$$

where, n_j is the product date, which refers to the serial number of the current date of the aerostat in a year, set from 0 to 365. The calculation formula of direct solar radiation Q_{suns} is as follows:

$$Q_{sun,i} = \lambda_z\alpha_{skin,i}\tau_{atm}I_0cos\beta_1 A_{skin,i} \tag{15}$$

where subscript i represents the i-th envelope unit; λ_z is the shielding coefficient, 1 for envelope units without direct sunlight, and 0 for vice versa. $\alpha_{skin,i}$ is the effective absorption coefficient of the i-th surface envelope unit of the near-space airship under direct solar radiation; τ_{atm} is solar radiation transmittance in the atmosphere [18].

2.2.4. Sky Radiation

When solar radiation passes through the atmosphere, it will scatter because of the gas and dust in the atmosphere, and this radiation is called sky radiation. The scattered radiation from the sky is independent of direction and is more intense when it is cloudy. The sky radiation can be calculated by the following formula:

$$I_{skysa} = \frac{I_0sin\alpha}{2}\frac{M(1 - \tau_{atm})}{M - 1.4ln\tau_{atm}} \tag{16}$$

The sky radiation can be obtained:

$$Q_{sky,i} = \alpha_{skin,i}I_{suns}\left(\frac{1 - cos\beta_2}{2}\right)A_{skin,i} \tag{17}$$

2.2.5. Reflected Radiation from the Earth and Clouds

Part of the radiation received by the surface of the near-space airship is the energy reflected by the radiation through the ground or clouds, this part of the radiation is called ground and cloud reflection radiation. The calculation formula of reflected radiation intensity of ground and cloud is as follows:

$$I_g = \rho_g(I_ssin\alpha + I_{sunsa}) \tag{18}$$

$$I_s = \tau_{atm} I_0 \tag{19}$$

where ρ_g represents the average reflectance of ground and cloud, and the reflectance is different for different landforms and targets, such as water surface, grassland, desert and snow field. For cloud reflectivity, it is 0.2 on sunny days and 0.6 on cloudy days. For different landforms, the surface reflectance is also different. For example, the reflectance of desert landform is 0.25, and that of snow field is 0.8. In general, the average surface and cloud reflectance of urban areas is 0.4.

The ground and clouds reflect radiation:

$$Q_g = \alpha_{skin} I_g \left(\frac{1 + cos\beta_2}{2} \right) A_{skin,i} \tag{20}$$

2.3. Analysis Process and Method

The calculation flow diagram of the coupled model is shown in Figure 3. First, the thermal model of the near-space airship was compiled into a UDF subroutine. After being called by FLUENT, the temperature field and aerodynamic load of the airship, considering the natural convection inside and outside the envelope, could be calculated. After interpolation mapping, the finite element model is formed. On the other hand, the biaxial tensile test data considering temperature were obtained, and the mechanical characteristics parameters of the envelope were presented considering the influence of temperature, stress magnitude and stress ratio. These mechanical parameters are compiled into the VFABRIC subroutine. After being called by ABAQUS, the fluid–solid–thermal coupling model can be calculated. For the ABAQUS coupling model at a certain time, the computation time takes 8 hours.
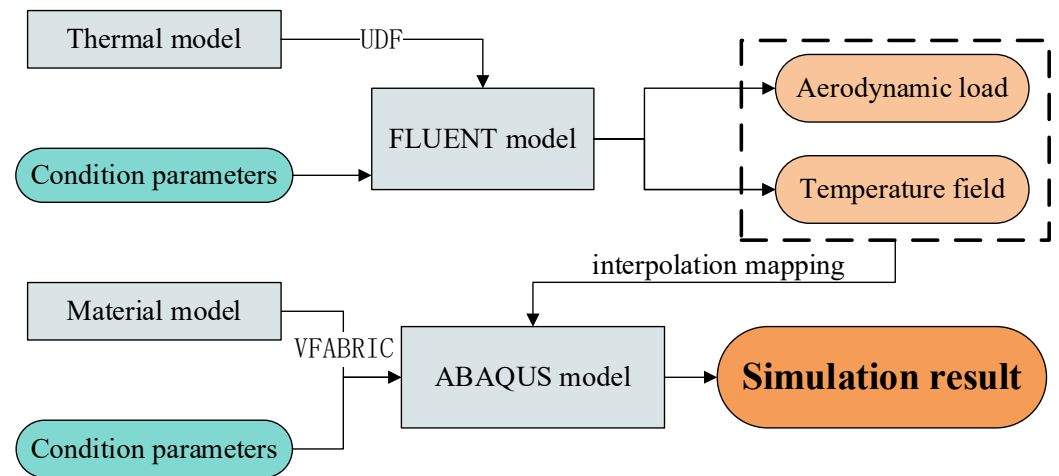

Figure 3. Analysis flow.

3. Coupling Model Condition

A fluid–solid–thermal coupling model of an airship with a length of 140 m and a maximum diameter of 36 m is provided, as shown in Figure 4. The finite element model is composed of 123,101 membrane elements, including 122,493 M3D4R elements and 1212 M3D3 elements. The airship simulates the fluid pressure difference P_f, buoyancy F_w, total weight G, pressure difference ΔP and heat distribution of the envelope surface under the real environment.

In this study, the local longitude and latitude, day of the year, altitude and attitude angle of the airship under certain environmental conditions are assumed. That is, assume that the airship is flying under the conditions shown in Table 2, with the head pointing east and maintaining the same attitude.

Figure 4. Coupling model.

Table 2. Parameters of the simulation environment.

Local latitude	41°	Local longitude	92°
Day of year	174	Altitude	20,000 m
Pitch angle of the airship	0°	Yaw angle of the airship	0°
Roll angle	0°	Inflow velocity	10 m/s

3.1. Boundary Condition

The boundary condition of the model is that the tailing of the airship does not limit the displacement of the weft direction, and the other five degrees of freedom are fixed; the head of the airship is fixed.

The following conditions are met when the airship is stationary(units: N):

$$F_w = G \tag{21}$$

where F_w is buoyancy, and G is gravity.

3.2. Buoyancy Condition

The calculation formula of buoyancy F_w:

$$F_w = \sum \Delta P_{wi} S_i \tag{22}$$

where S_i is the area of the airship unit, and ΔP_{wi} is the pressure on the inner surface of each cell of the envelope. The calculation method is as follows:

$$\Delta P_{wi} = (\rho_a - \rho_{He}) \Delta y_i g \tag{23}$$

where ρ_a is the air density at the flying altitude of the airship, ρ_{He} is the helium density at the flying altitude of the airship, Δy_i is the height difference between the airship unit and the lowest point unit in the gravity direction of the airship. g is the acceleration of gravity.

3.3. Aerodynamic Load Condition

The general view of the computational domain and mesh distribution around the airship is illustrated in Figure 5. As shown in Figure 5a, the whole domain is a rectangle of 180 hull length long and 180 hull length wide. Figure 5b shows the close view of the mesh domain around the airship. The height of the first row mesh is set such that the y+ is equal to 1 [30]. The mesh dependency study is made and the unstructured mesh number of 2,178,168 is finally applied.
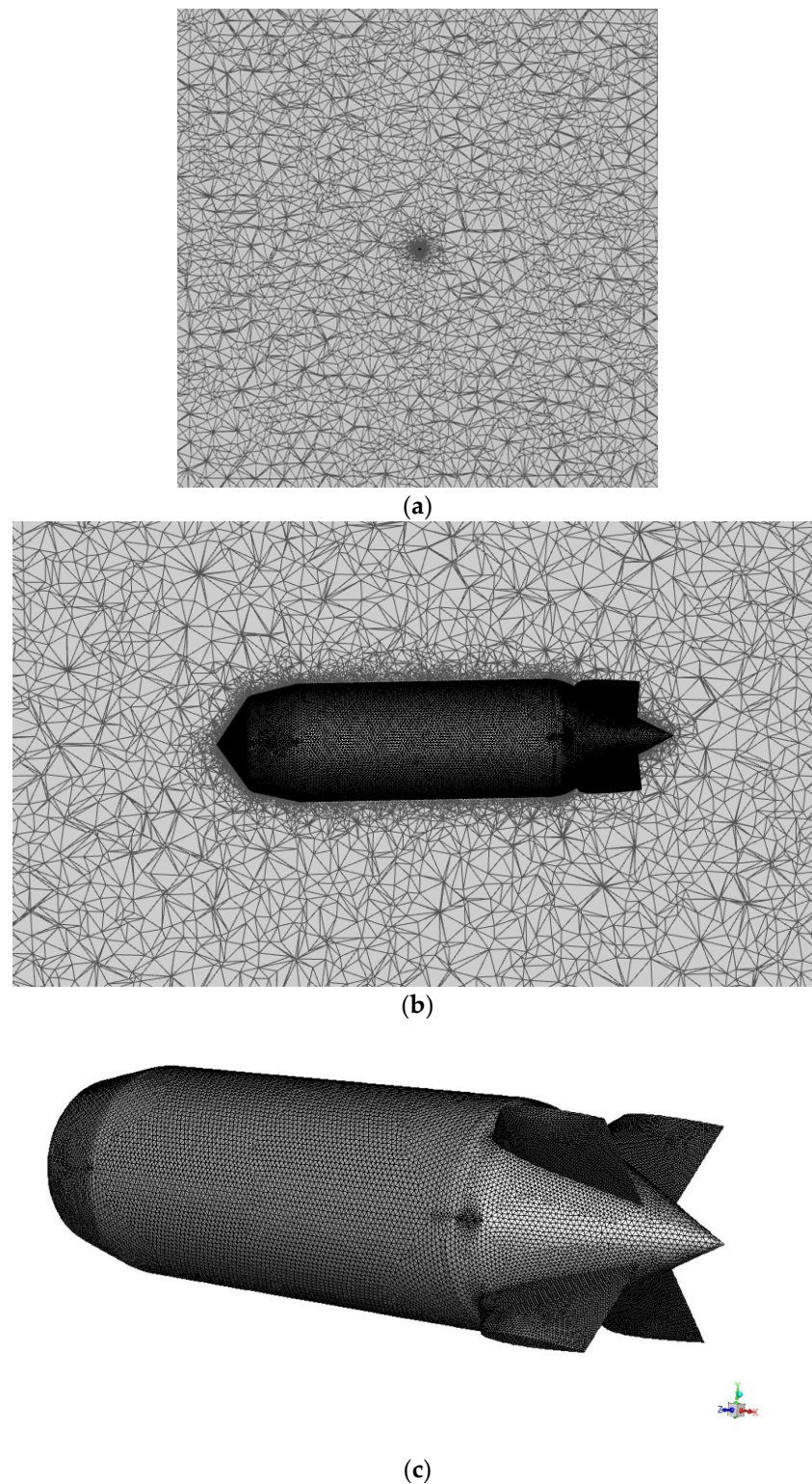
(a)

(b)

(c)

Figure 5. Fluid mesh condition of the airship. (**a**) Domain condition. (**b**) Mesh domain around the airship. (**c**) The surface mesh of the airship.

A three-dimensional incompressible unsteady CFD solver in the commercial software FLUENT 14.0 is adopted to solve the RANS governing equations. Due to the incompressibility of the flow, the pressure-based solver is utilized, which has a good capability of solving the low-speed incompressible flows. The RANS governing equations are solved implicitly [31] and the SIMPLE algorithm is taken as the pressure-velocity coupling ap-

proach. The Green-Gauss Node-based method [32] is adopted in gradient interpolation. The convective flux terms and diffusive flux terms are discretized with the second-order accurate upwind scheme [32] and second-order accurate central difference scheme [33], respectively. The velocity inlet and pressure outlet boundary condition are adopted.

The aerodynamic load of the airship is mainly caused by the flow of external air relative to the airship envelope, and the natural convection inside the airship envelope also produces the corresponding load. In the calculation results, the cloud diagram of the external forced convection load distribution of the envelope is shown in Figure 6a. According to the aerostatic load cloud diagram of the envelope, the aerostatic pressure on the head and tail of the airship is greater than zero, indicating that the envelope is subjected to pressure from the outside to the inside under this working condition. The tail of an airship is sometimes affected by the wake vortex and produces positive static pressure. In the direction from the head to the tail of the airship, the static pressure of the head of the envelope is distributed from large to small, and the maximum value is 4.0 Pa, while the maximum value of the tail is 1.7 Pa. Except for the head and tail region, the pressure on the other envelopes is from inside to outside, and the pressure at the first turning point near the head of the outer envelope is the largest, which is 5 Pa. The hull's static pressure from inside out is 0.3 to 0.5 Pa. The cloud diagram of load distribution generated by natural convection inside the envelope is shown in Figure 6b, in which the hull is subjected to negative pressure.
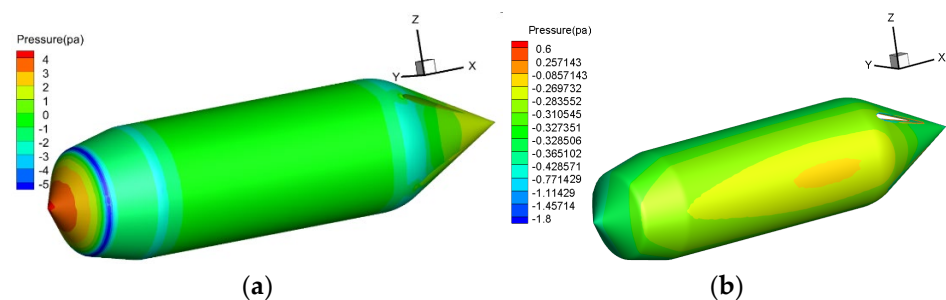

(**a**)   (**b**)

Figure 6. Static pressure of the envelope. (**a**) Forced convection pressure. (**b**) Natural convection pressure.

4. Results and Discussions

4.1. Simulation Results

The fluid–solid–thermal coupling of an airship in 24 hours is analysed, and the stress–strain distribution and heat distribution results under corresponding conditions are obtained. Here, the corresponding simulation results at 6:00 a.m., 12:00 p.m., 6:00 p.m. and 12:00 a.m. are selected for analysis and explanation. The internal pressure of the airship is set as 300 Pa; that is, the simulation assumes that the airship works in a controlled constant pressure environment, and its attitude remains unchanged. According to the thin-shell cylinder theory, δ_m = 16.875 Mpa and δ_θ = 33.75 Mpa are calculated. Where δ_m is the axial stress, and δ_θ is the circumferential stress.

4.1.1. Simulation Results at 6:00 a.m.

The temperature distribution diagram of the envelope surface at 6:00 a.m. on the summer solstice is shown in Figure 7a. At this time, the highest temperature of the envelope surface is mainly concentrated at the head of the airship, and the overall temperature is at a low level. Due to the sunrise and the orientation of the airship, the highest temperature on the surface of the airship envelope is mainly concentrated at the airship head, the lowest temperature at the tail, and the temperature distribution of the body is more uniform.
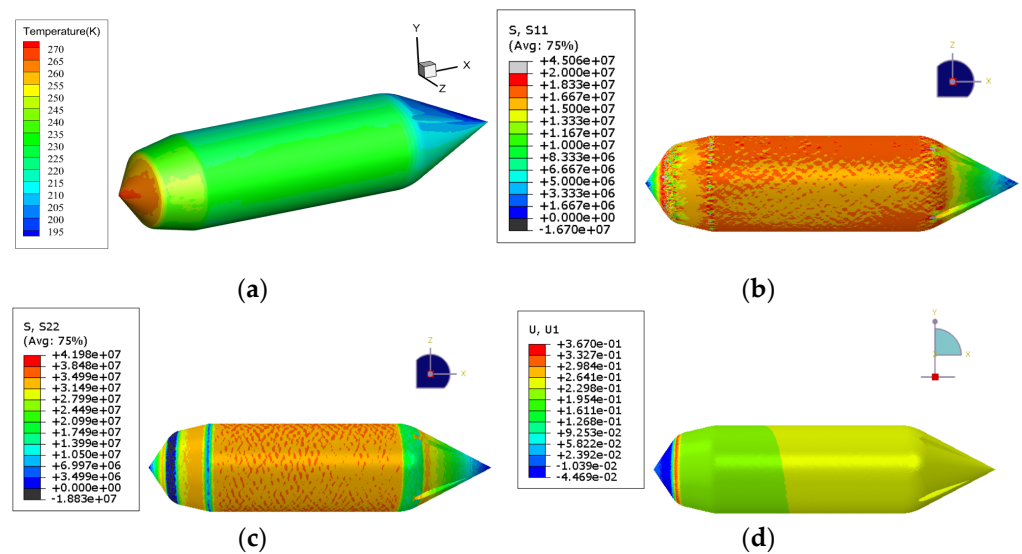
Figure 7. Simulation results at 6:00 a.m. (**a**) Temperature distribution at 6:00 a.m. (**b**) S11 stresses at 6:00 a.m. (units: Pa) (**c**) S22 stresses at 6:00 a.m. (units: Pa) (**d**) U1 deformation at 6:00 a.m. (units: m).

The stress cloud diagram of S11 at this time is shown in Figure 7b. The maximum value of S11 is distributed at the top of the airship, the stress on both sides of the ship is relatively uniform, and the head and tail of the ship are small. The S11 stress of the hull is between 16 Mpa and 20 Mpa, which is similar to the axial stress δm of a thin-shell cylinder.

As shown in Figure 7c, the S22 stress at the turning point of the envelope near the head of the airship is more complex than other parts, with a negative value of S22. The S22 stress of the hull is greater than that of the head and tail, and the S22 stress of the hull half is higher than that of the lower part.

As shown in Figure 7d, at 6:00 a.m., the head of the airship expands negatively in the axial direction, while other parts expand positively in the axial direction. According to the gradient line of the cloud image, under the influence of buoyancy, gravity, aerodynamic force, pressure difference and temperature, the deformation of the airship in the axial direction is not uniform but gradually changes with the circumferential and axial direction at the same time. The largest deformation occurs at the shape turning point of the envelope near the airship head, mainly because of the depression deformation.

4.1.2. Simulation Results at 12:00 p.m.

Figure 8a shows the temperature distribution of the envelope surface at 12:00 p.m. on the summer solstice. Affected by direct solar radiation, convective heat transfer outside the envelope, reflected radiation from the ground and clouds, and long-wave radiation from the sky, the overall temperature is at a high level. At this time, the highest temperature of the airship body transferred to the second half of the ship and the tail.

At 12:00 p.m., the airship envelope outer surface temperature reached the maximum value in a day, concentrated on the top of the middle part of the ship. Figure 8b shows the axial stress distribution of the outer envelope of the near-space airship. The axial stress at the bottom of the hull is slightly lower, and the S11 stress of the whole hull is 16–20 Mpa.

At 12:00 p.m., the stress distribution of the near-space airship's outer envelope is shown in Figure 8c. The higher stress is high in a circumferential direction, mainly concentrated in the middle of the hull, higher than the airship's head and tail.

The deformation and displacement distribution of the outer envelope at 12:00 p.m. is shown in Figure 8d. Due to the high temperature in the upper part of the airship at this time, the Young's modulus of the envelope decreases, resulting in the deformation of the upper part of the envelope being larger than that of the lower part, so a gradient line from the upper right to the lower left appears in the cloud image.
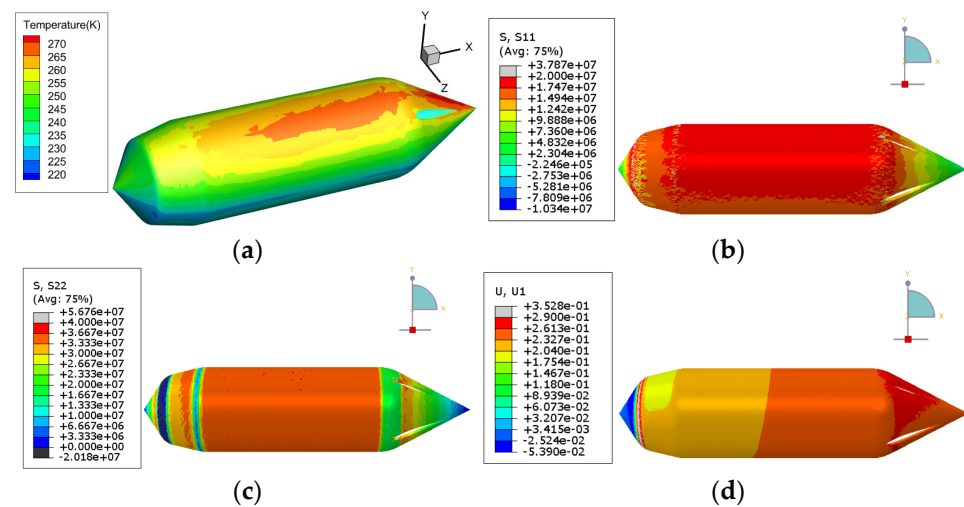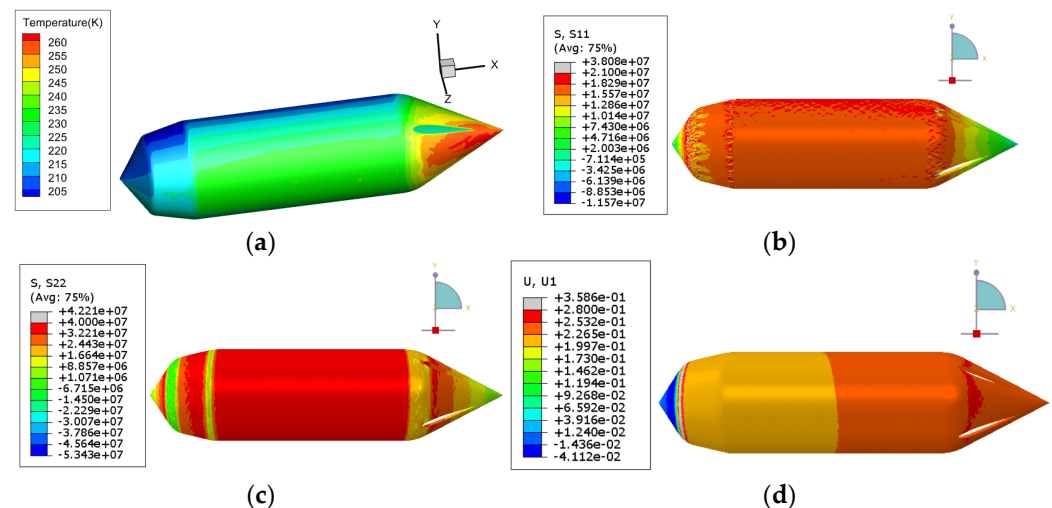
Figure 8. Simulation results at 12:00 p.m. (**a**) Temperature distribution at 12:00 p.m. (**b**) S11 stresses at 12:00 p.m. (units: Pa) (**c**) S22 stresses at 12:00 p.m. (units: Pa) (**d**) U1 deformation at 12:00 p.m. (units: m).

4.1.3. Simulation Results at 6:00 p.m.

Figure 9a shows the temperature distribution of the envelope surface at 6:00 p.m. During this period, the direct solar radiation, ground and cloud radiation weaken, and the overall temperature is about to drop sharply. At this time, the highest temperature of the airship body is concentrated at the airship tail, and the temperature of the ship head and hull decreases.
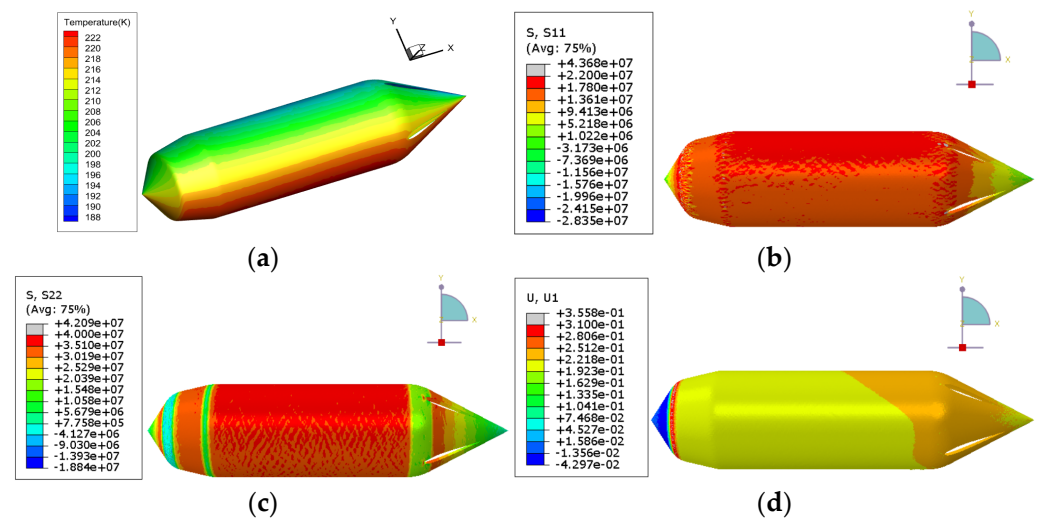

Figure 9. Simulation results at 6:00 p.m. (**a**) Temperature distribution at 6:00 p.m. (**b**) S11 stresses at 6:00 p.m. (units: Pa) (**c**) S22 stresses at 6:00 p.m. (units: Pa) (**d**) U1 deformation at 6:00 p.m. (units: m).

Figure 9b shows the axial stress distribution of the outer envelope of the near-space airship. The high stress on the envelope gathers most of the middle part of the hull, the axial stress on the top of the hull is slightly higher, and the S11 stress of the whole hull is 16.5–19 Mpa. S11 in the tip of the airship head and tail is less stressed.

At 6:00 p.m., the circumferential direction stress distribution of the near-space airship outer envelope is shown in Figure 9c. The high stress is mainly concentrated in the middle part of the hull, which is higher than the head and tail.

At 6:00 p.m., the distribution of U1 deformation and displacement of the outer envelope of the near-space airship is shown in Figure 9d. Different from the previous time, the

displacement gradient line in the cloud image changed from upper left to lower right due to the change in temperature distribution on the surface of the envelope. It shows that the lower part of the airship envelope deformation degree is higher than the upper part when the airship enters the evening.

4.1.4. Simulation Results at 12:00 a.m.

Figure 10a shows the temperature distribution of the envelope surface at 12:00 a.m. on the summer solstice. At this time, the surface temperature of the airship envelope enters a relatively stable stage, mainly affected by earth long-wave radiation and sky long-wave radiation. The maximum temperature of the airship is distributed in the lower part of the body, and the temperature of the body is lower.

Figure 10. Simulation results at 12:00 a.m. (**a**) Temperature distribution at 12:00 a.m. (**b**) S11 stresses at 12:00 a.m. (units: Pa) (**c**) S22 stresses at 12:00 a.m. (units: Pa) (**d**) U1 deformation at 12:00 a.m. (units: m).

At 12:00 a.m., the axial direction stress (S11) distribution of near-space airship outer envelope S11 is shown in Figure 10b. Compared with the radial stress of the envelope at 12:00 p.m., the stress of the airship envelope at this time is more uniform, and the overall stress is larger. The S11 stress of the envelope in the middle part of the hull is between 16.5 Mpa and 19 Mpa.

The circumferential direction stress (S22) distribution of the near-space airship outer envelope is shown in Figure 10c. The circumferential direction stress of the lower part of the hull is lower on the whole. The S22 stress of the airship's head and the tail is lower than that of the middle hull. According to the S22 stress distribution of the envelope at 12:00 a.m., the S22 stress in the middle of the hull is 30–37 Mpa.

The distribution of U1 deformation and displacement of the outer envelope of the near-space airship is shown in Figure 10d. At this time, the expansion of the head of the airship produces a negative X-axis displacement, and the temperature of the lower part of the airship is higher than that of other regions under the influence of reflected radiation from the ground and clouds, and the Young's modulus of the envelope decreases, resulting in the deformation of the lower part of the airship envelope material is larger than that of the upper part, and a gradual curve from the upper left to the lower right appears in the cloud image.

From the analysis of stress and deformation characteristics of the stratosphere airship at different times (24 h) above, it can be seen that the stress on the top of the middle part of the outer envelope is generally high, and more attention should be paid to the strength and safety of the envelope body in this area. The axial and circumferential stresses in the middle part of the airship envelope are not different from the theoretical values. Generally

speaking, the stress distribution in the bow and stern is small, but attention should be paid to the area around the shape bend of the airship. Because of the sagging phenomenon in this area, the circumferential frame can be arranged in practical engineering applications. In addition, the gradient lines in the deformation and displacement cloud map show that the fluid–solid–thermal coupling finite element model established in this paper can predict the shape deformation of airship envelope under different temperature fields.

4.2. Volume Change of Airship Envelope under Fluid–Solid–Thermal Coupling

Figure 11 shows the volume and length changes of the airship simulated under fluid–solid–thermal coupling on the summer solstice. Refer to Section 3 for setting the corresponding environment parameters; the internal pressure is 300 Pa and 500 Pa, respectively. Among them, the original volume of the airship is 107,800 m^3, and the length is 140 m.
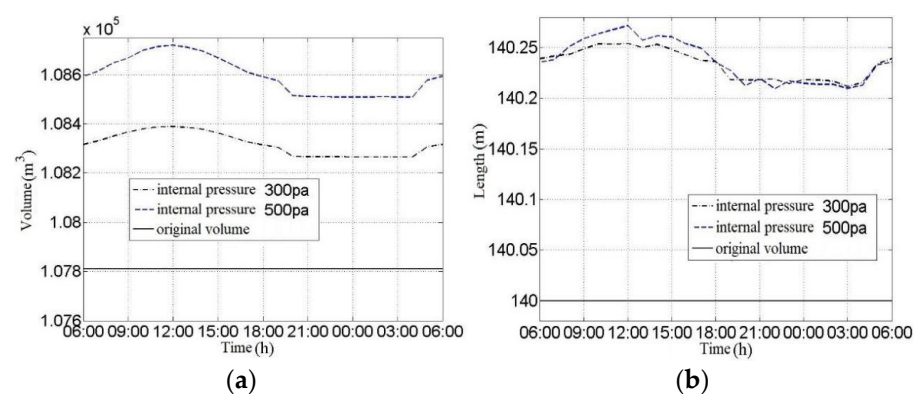

Figure 11. Changes in airship volume and length. (**a**) Airship volume. (**b**) Airship length.

It can be seen from Figure 11a that the volume variation trend is similar to the direct solar radiation, indicating that the volume of the airship is greatly affected by direct solar radiation when it works under certain working conditions. When the airship reaches its maximum volume at 12:00 p.m., the volume drops sharply from 19:00 to 20:00 and reaches a plateau at 21:00. At this time, the temperature distribution and volume value of the airship envelope are relatively fixed. The maximum volume difference between day and night is 124.223 m^3 at 300 Pa and 210.922 m^3 at 500 Pa. Under different internal pressure conditions, high internal pressure has a greater influence on the volume of the airship.

As shown in Figure 11b, the total length of the airship also shows a similar trend with the change in temperature and volume. The airship reaches the maximum length at 12:00 p.m., then decreases, and begins to reach the minimum length in the evening. It is worth noting that the influence of internal pressure on the length of an airship is not particularly great; the maximum appeared at 12:00 p.m.; at this time, the length of the internal pressure of 500 Pa is 0.0178 m longer than that of 300 Pa. However, the volume of the airship at 500 Pa is 330.4518 m^3 larger than that at 300 Pa, indicating that the influence of internal pressure on the volume of the airship is mainly caused by the expansion and contraction of the airship envelope rather than the change of the airship length.

According to the changing trend of near-space airship volume over time, the simulation results of airship deformation at 12:00 p.m. and early morning are taken as objects, and the shape extraction of the airship in XY view is shown in Figure 12. The shape of the airship in the picture has been enlarged or reduced by 10% relative to the original shape to better observe the changes. The Y-axis in the figure is the direction of gravity on the airship. Compared with the early morning, the near-space airship at 12:00 p.m. not only has a larger shape but also has a larger upward expansion of the whole envelope, and the expansion of the aft part of the ship is more obvious than the bow part, the length of the ship becomes longer, and the head part shrinks.
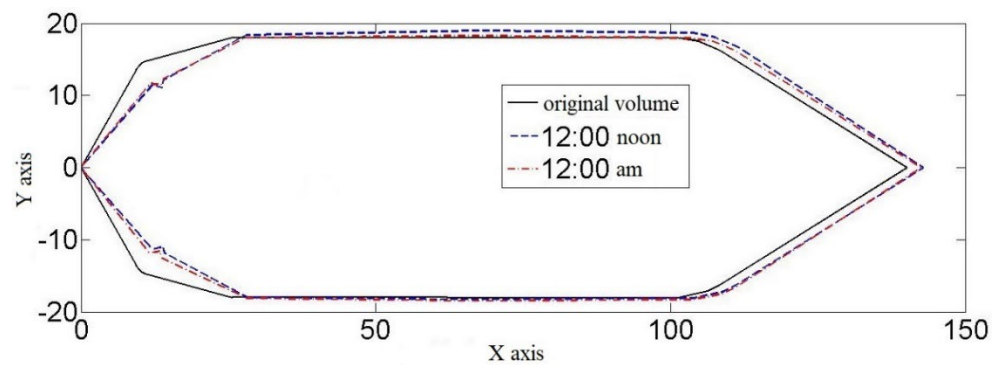
Figure 12. The comparison of airship shapes (X-Y view) (units: m).

Figure 13 shows the shape of the near-space airship envelope after deformation in XZ view. According to the deformation curves of airships in XY and XZ views, although the head of the airship at 12:00 p.m. is smaller than that at 12:00 a.m. in the gravity direction (Y-axis direction), the head of the airship at 12:00 p.m. is larger than that at Z-axis direction. This indicates that the YZ cross-section of the airship's outer envelope is no longer a regular circle under the influence of temperature at different moments. Relative to the original shape of the airship, affected by temperature and load, the head shrinks, the hull and tail expand, and the length increases. For the airship, in this case, there is a depression at the turning point of the outer envelope close to the head, which has already appeared in the stress and deformation analysis of the envelope. This is caused by the lengthening of the airship envelope and the expansion of the airship hull. For this phenomenon, it is necessary to add a fixed ring at this part to maintain the shape of the airship.
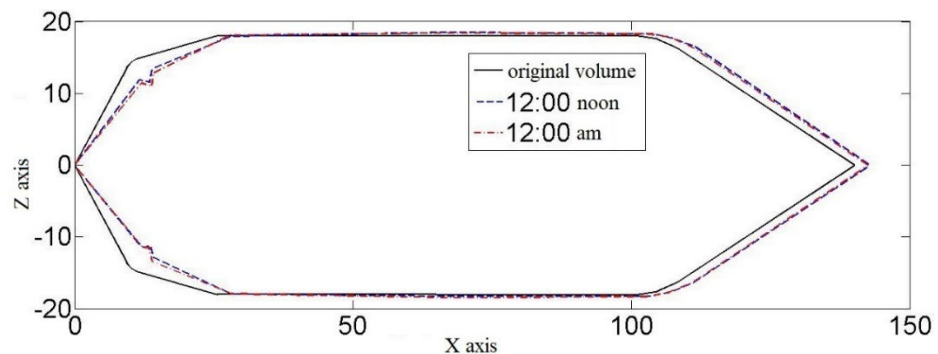

Figure 13. The comparison of airship shapes (X-Z view) (units: m).

5. Conclusions

The unidirectional fluid–solid–thermal coupling model of the outer stratospheric envelope is established with CFD and the structural finite element method. Based on the high and low temperature biaxial tensile test data, the fluid–solid–thermal coupling calculation and analysis is realised considering factors such as the anisotropy of the envelope material, the temperature and Young's modulus change. The temperature difference and stress–strain behaviour of the near-space airship envelope were simulated and predicted, and the force and deformation law under the influence of fluid–solid–thermal coupling was analysed. The main conclusions are as follows:

(1) The total length of the airship shows a similar trend with the change in temperature and volume. The influence of internal pressure on the length of an airship is not particularly great, which indicates that the influence of internal pressure on the volume of the airship is mainly caused by the expansion and contraction of the airship envelope rather than the change of the airship length.

(2) At noon, the stress near the upper half of the airship body generally increased due to the high temperature of the airship. And both in day and night, the maximum stress is always concentrated in upper half of the airship.

(3) The proposed finite element model can effectively predict the variations of the stress distribution, temperature distribution, and shape deformation with regions and time, under the fluid-solid-thermal coupling effects.

References

1. Tang, J.; Duan, D.; Xie, W. Shape Exploration and Multidisciplinary Optimization Method of Semirigid Nearing Space Air-ships. *J. Aircr.* **2021**, *59*, 946–963. [CrossRef]
2. Tang, J.; Wang, X.; Duan, D.; Xie, W. Optimisation And Analysis Of Efficiency For Contra-Rotating Propellers for High-Altitude Airships. *Aeronaut. J.* **2019**, *123*, 706–726. [CrossRef]
3. Stefan, K. Thermal effects on a high altitude airship. In Proceedings of the American Institute of Aeronautics and Astronautics 5th Lighter Than Air Conference, Anaheim, CA, USA, 25–27 July 1983.
4. Cathey, H.M., Jr. *Advances in the Thermal Analysis of Scientific Balloons*; Springer: Berlin/Heidelberg, Germany, 2006.
5. Garde, G. Thermal Modeling of NASA's Super Pressure Pumpkin Balloon. In Proceedings of the AIAA Balloon Systems Conference, Williamsburg, VA, USA, 8 May 2013.
6. Fang, X.D.; Wang, W.Z.; Li, X.J. A Study of Thermal Simulation of Near-space airships. *Spacecr. Recovery Remote Sens.* **2007**, *28*, 5–9.
7. Xu, X.H.; Cheng, X.T.; Liang, X.G. Thermal analysis of a near-space airship. *J. Tsinghua Univ. (Sci. Technol.)* **2009**, *49*, 1848–1851.
8. Liu, D.; Yang, Y.; Lü, M.; Wu, Z. Effect of envelope thermal radiative properties on the stratospheric super-pressure LTA vehicle helium temperature. *J. Beijing Univ. Aeronaut. Astronaut.* **2010**, *36*, 83–87.
9. Xia, X.L.; Li, D.F.; Sun, C.; Ruan, L.M. Transient Thermal Behavior of Stratospheric Balloons at Float Conditions. *Adv. Space Res.* **2010**, *46*, 1184–1190. [CrossRef]
10. Wang, Y.W.; Yang, C.X. A Comprehensive Numerical Model Examining the Thermal Performance of Airships. *Adv. Space Res.* **2011**, *48*, 1515–1522. [CrossRef]
11. Dai, Q.M. *Research on the Thermal Environment and Thermal Characteristics for Aerostats*; Nanjing University of Aeronautics and Astronautics: Nan Jing, China, 2014.
12. Liu, T.T.; Ma, Z.Y.; Yang, X.X.; Zhang, J.S. Influence of Solar Cells On Thermal Characteristics of Near-Space Airship. *J. Astronaut.* **2018**, *39*, 35–42.
13. Harada, K.; Eguchi, K.; Sano, M.; Sasa, S. Experimental Study of Thermal Modeling for Stratospheric Platform Airship. In Proceedings of the AIAA's 3rd Annual Aviation Technology, Integration, and Operations (ATIO) Forum, Denver, CO, USA, 17–19 November 2003.
14. Cheng, X.T.; Xu, X.H.; Liang, X.G. Thermal Simulation and Experiment for an Airship under Low Altitude Environment. *J. Astronaut.* **2010**, *31*, 2417–2421.
15. Bruce, R.; Reulet, P.; Millan, P.; Parot, G.; Letrenne, G. Experimental Study of Natural Convection on the Wall of Infrared Balloon. In Proceedings of the 10th AIAA/ASME Joint Thermo-physics and Heat Transfer Conference, Chicago, IL, USA, 28 June 2010.
16. Li, D.F. *Thermal Behavior and Its Dynamic Effects on Stratospheric Aerostats*; Harbin Institute of Technology: Harbin, China, 2011.
17. Carlson, L.A.; Horn, W.J. New Thermal and Trajectory Model for High-Altitude Balloons. *AIAA Pap.* **1981**, *20*, 500–507.
18. Rodger, F. Balloon Ascent: 3-D Simulation Tool for the Ascent and Float of High-Altitude Balloons. In Proceedings of the AIAA 5th ATIO and 16th Lighter-Than-Air System Technology and Balloon Systems Conferences, Arlington, VA, USA, 26–28 September 2005.

19. Yao, W.; Lu, X.; Wang, C.; Ma, R. A Heat Transient Model for the Thermal Behavior Prediction of Near-space airships. *Appl. Therm. Eng.* **2014**, *70*, 380–387. [CrossRef]
20. Dai, Q.; Fang, X.; Li, X.; Tian, L. Performance Simulation of High Altitude Scientific Balloons. *Adv. Space Res.* **2012**, *49*, 1045–1052. [CrossRef]
21. Zheng, W.; Zhang, X.; Ma, R.; Li, Y. A Simplified Thermal Model and Comparison Analysis for a Stratospheric Lighter-Than-Air Vehicle. *J. Heat Transf. Tranenvel. ASME* **2018**, *140*, 022801. [CrossRef]
22. Cheng, C. *Transient Thermal Model and Thermal Characteristics Analysis of Near-Space Airships*; Shanghai Jiao Tong University: Shanghai, China, 2019.
23. Wang, X.L.; Xie, W.C. Thermal Characteristics Analysis of Near-space airships Envelope. *Equip. Environ. Eng.* **2020**, *17*, 13–19.
24. Wang, X.L.; Shan, X.X.; Chen, L. Study on Fluid-Structure Coupled Computational Method for Stratosphere Airship. *J. Astronaut.* **2011**, *32*, 22–28.
25. Bessert, N.; Frederich, O. Nonlinear Airship Aeroelasticity. *J. Fluids Struct.* **2005**, *21*, 731–742. [CrossRef]
26. El Omari, K.; Schall, E.; Koobus, B.; Dervieux, A.; Amara, M.; Dumas, J.P. Fluid-Structure Coupling of a Turbulent Flow and a Generic Blimp Structure at High Angle of Attack. *Ninth Int. Conf. Zaragoza Pau Appl. Math. Stat.* **2006**, *33*, 369–376.
27. Liu, J.M. *Coupling Computation of the Flow Field and the Large Deformation of Membrane Structure of Stratosphere Airships*; Shanghai Jiao Tong University: Shanghai, China, 2007.
28. Dai, Q.M.; Fang, X.D. Thermal-fluid-Structure Coupling analysis on Near-space airships. In Proceedings of the 5th China High Resolution Earth Observation Conference, Xi'an, China, 18–20 June 2018.
29. Jenkins, E.P. Principles of Solar Engineering. *Sol. Energy* **1979**, *23*, 183–184. [CrossRef]
30. Nobile, R.; Vahdati, M. Dynamic Stall for a Vertical Axis Turbine in a Two-Dimensional Study. In Proceedings of the World Renewable Energy Congress, Lisbon, Portugal, 26–30 July 2011.
31. Yang, Y.; Li, D.; Zhang, Z.H. Influences of Flapping Wing Micro Aerial Vehicle Unsteady Motion on Horizontal Tail. *Acta Aeronaut. Astronaut. Sin.* **2012**, *33*, 1827–1833.
32. Shima, E.; Kitamura, K.; Haga, T. Green-Gauss/Weighted-Least-Squares Hybrid Gradient Reconstruction for Arbitrary Polyhedra Unstructured Grids. *AIAA J.* **2013**, *51*, 2740–2747. [CrossRef]
33. Warming, R.F.; Beam, R.M. Upwind Second-Order Difference Schemes and Applications in Aerodynamic Flows. *AIAA J.* **1976**, *14*, 1241–1249. [CrossRef]